Mach 6 Testing of a Scramjet Engine Model*

Takeshi KANDA*1, Toshihito SAITO*1, Kenji KUDO*1,
Tomoyuki KOMURO*1 and Fumiei ONO*1

Abstract

Testing of a sub-scale scramjet research engine model was carried out in the March 6 Ramjet Engine Test Facility of the National Aerospace Laboratory, Kakuda Research Center. By attaching a short strut on the top wall, intensive combustion with high combustion efficiency was attained, and the engine-produced thrust canceled the drag. The flame was held in the low-velocity region around the step, even after the ignitors had been turned off. When the fuel flow rate was small, there was a different combustion mode with weak combustion and little thrust. Tangential injection of fuel intensive combution.

Keyword : scramjet, supersonic combustion, supersonic flow

概　　要

角田宇宙推進技術センターにおいてラムジェットエンジン試験設備の飛行マッハ数６条件下で，スクラムジェットサブスケールエンジンの試験を行った。天板に短ストラットを取り付けることにより，良好な燃焼状態および高い燃焼効率が達成され，燃焼により発生した推力は流入気流による抗力に匹敵した。良好な燃焼が達成された後は，着火・保炎用のプラズマジェットを切った後も燃焼が持続した。燃料流量が少ない場合には別の燃焼モードが現れ，燃料は僅かに燃焼したに過ぎなかった。ステップからの燃料の平行噴射は良好な燃焼状態を阻害した。

1. Introduction

Study of an aerospace plane is being carried out to create a new transportation system to low earth orbit. One of the engines that will be used in the aerospace plane, the scramjet, is being studied at the National Aerospace Laboratory, Kakuda Research Center (NAL, KRC), and a sub-scale scramjet research engine model has been tested under Mach 4 and Mach 6 flight conditions in the Ramjet Engine Test Facility (RJTF) at the center[1,2].

In a previous test under Mach 6 flight condition, the engine did not produce thrust. To enhance combustion, a short strut was attached to the top wall of the engine. This modification was expected to increase the pressure, decelerate the air, enhance the mixing, and create a re-circulation region near the ignitors and the backward-facing step for flame holding. The results of the testing with the short strut are herein presented.

2. Experimental Apparatus and Methods

2.1 Test facility

The test conditions in the RJTF are shown in Table 1. They correspond to the flight conditions of Mach 6 with a flight dynamic pressure of 64 kPa. Compressed air was heated by a ceramic storage heater. The supersonic nozzle had exit dimensions of 51 cm by 51 cm. The boundary layer thickness was 58 mm, and the displacement thickness was 20 mm at the en-

Table 1　Testing conditions

Mach number	5.30
Total temperature, K	1550
Total pressure, kPa	4780

＊　Received 5 June 1997（平成９年６月５日受付）

＊1　Ramjet Propulation Research Division, Kakuda Research Center
（角田宇宙推進技術研究センター，ラムジェット推進研究部）

gine entrance according to pitot pressure measurement[3].

2.2 Engine model

Figure 1 shows a schematic diagram of the engine model. In the present testing, the engine had a short strut on the top wall. Its height was 50 mm, one-fifth that of the engine model. The engine had a side wall compression-type inlet, and the contraction ratio was three. There was a duct with a constant cross section area between the inlet and the combustor, which acted as an isolator. The model had two plasma ignitors[4], each with 2.5 kW power. It employed oxygen as its working gas. There was no fuel injection from the strut. There was a backward-facing step between the isolator and the combustor for both flame holding and isolation of pressure increase in the combustor. Its height, h, was 4 mm on the side walls, and 2 mm on the top wall.

The fuel, hydrogen, was injected normal to the side walls through 24 holes, or tangentially to the side walls through 24 holes on the steps. Their throat diameter was 1.5 mm. The total temperature of the fuel was approximately 280 K, and the total pressure of the fuel varied from 3.6 to 6.3 MPa, according to the fuel flow rate. The pilot fuel was supplied through 6 holes on the top wall and 94 holes on the side walls, the diameter of each being 0.5 mm. Fuel flow rates were measured by metering orifices. The difference of the fuel flow rates from the normal injection holes downstream of the step was estimated about 2 %. The difference was due to the dynamic pressure distribution in the manifold.

The engine was not cooled. Its walls consisted of tough pitch copper, and the leading edges of the side wall, the top wall, and the cowl were made of nickel. The inner surface of the top wall of the model coincided with that of the Mach 5.3 nozzle to ingest the boundary layer. The boundary layer occupied one-fifth of the engine height at the entrance of the engine. It simulated the entrance conditions of the engine of the aerospace plane.

2.3 Measurements

Wall pressure and wall temperature at 1 mm from the inner surface of the model were measured. In the present paper, the wall pressure, P_w, is non-dimensionalized with the total pressure, PO, in the reservoir of the wind tunnel of the RJTF. In the following figures, the pressure of the top wall was measured along the center line of the channel. The measurement error of non-dimensionalized wall pressure was $\pm$ 0.0001 in the inlet, in the divergent part of the combustor (D.C.), and in the nozzle, while it was $\pm$0.0005 in the isolator (Is.) and in the constant duct part of the combustor (C.C.).

Heat flux, q, was estimated from the rate of wall temperature change measured by thermo-couples. The Fourier number was about 0.5 in the present testing, so the heat flux was expressed as follows[5,6]:

$$q = \rho c \ell (dT/dt) \quad (1)$$

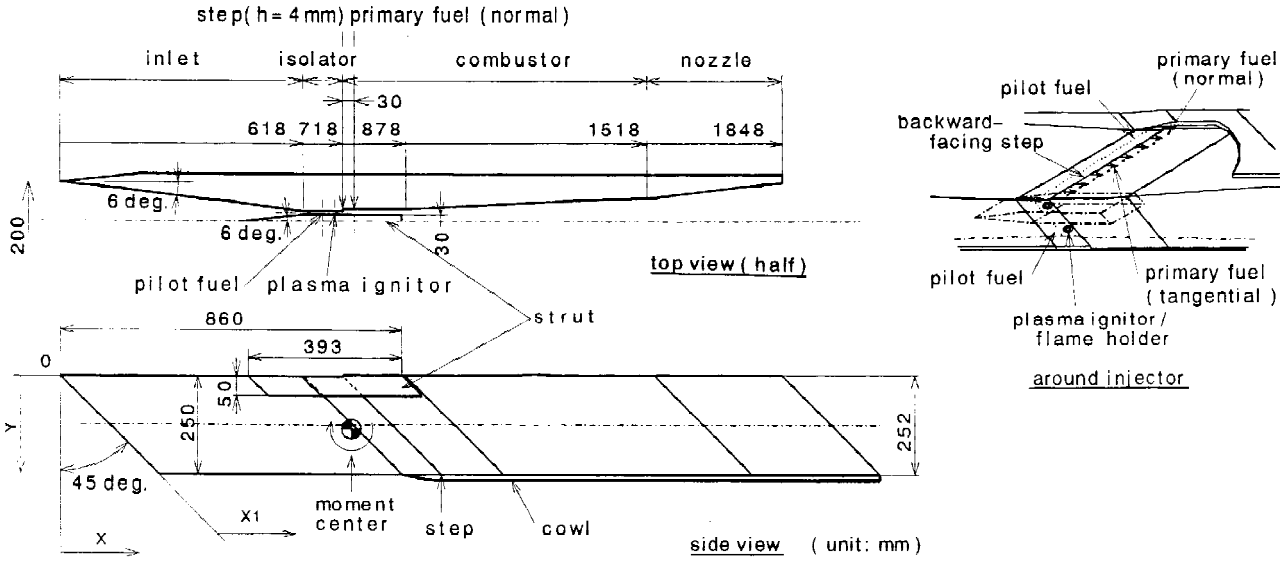

Fig. 1 Engine model.

Here, ρ, c, ℓ, T, and t denote density, specific heat, thickness of the wall, temperature, and time, respectively. The error of heat flux was $\pm$ 2.5% in the present testing.

Thrust, lift, and pitching moment were measured by a floating frame force measurement system (FMS). The error of forces was $\pm$50 N. The center of pitching moment was set at x = 741.43 mm and y = 135.8 mm as shown in Fig. 1. Here, the x coordinate is the distance from the origin as shown in Fig. 1, and the y coordinate is the distance from the top wall. The $x1$ coordinate is the distance from the leading edge of the side wall. The top wall was at y = 0 mm and the cowl surface was at y = 250 mm.

2.4 Fuel supply conditions

Nine tests from # 12 to # 20 were conducted in the present series. The fuel flow rates of the tests are listed in Table 2. The timing for opening of each fuel supply valve was different, so there were several kinds of fuel supply conditions in every test. The differences of combination of fuel flow rates in each test are represented by letters, and each test condition is expressed by the test number and a letter, e.g., #16d, # 19e, # 18d, etc. The operating condition with air flow only, i.e., with no fuel injection, is termed the reference condition. When there was fuel injection, the plasma ignitors were usually turned on.

3. One-Dimensional Calculation

Neither the pitot pressure measurement nor the gas sampling were carried out in the engine or downstream of the engine in the present testing. Therefore, a one-dimensional flow calculation model was constructed to investigate the test results and estimate the model engine performances, e.g., the Mach numbers in the engine model, the kinetic energy efficiency of the inlet, and the combustion efficiency. The assumptions and calculation conditions were as follows.

(1) In the engine model of the one-dimensional calculation, the effect of the swept angle was ignored, and the distance from the leading edge, $x1$, was used when the calculated results were compared with the experimental data.

(2) In the calculation model, a mass capture ratio of the inlet of 0.86 was chosen based on the spillage calculated by the two-dimensional shock wave relation and the measured boundary layer displacement thickness[3]. The definition of the mass capture ratio is as follows:

(Mass capture ratio) = (Air mass flow rate at exit of the inlet) / (Air mass flow rate with primary flow mass flux to the projected area at entrance of theengine)

(3) The stream thrust function of the spilled air was set equal to that of the incoming airflow[7].

(4) The air and the combustion gas were equilibrium flows through the engine.

(5) Modeling of mixing of fuel with the air was not done.

(6) The hydrogen burned all at once in a stoichiometric condition with the specified combustion efficiency at the specified location. The location of heat release was estimated by the measured heat flux and wall pressure. The residual hydrogen mixed with the residual air.

(7) The kinetic energy efficiency of the inlet and the

Table 2 Fuel flow rates

Test No.	Fuel flow rate ($g \cdot s^{-1}$)					Equivalence ratio
	Normal	Tangential	Top wall pilot	Side wall pilot	Total	Total
#12	86	0	3	42	131	0.86
#13	40	0	2	19	61	0.40
#14	53	0	2	10	65	0.43
#15	14	0	2	8	24	0.16
#16	26	0	2	8	36	0.24
#17	83	0	3	10	96	0.63
#18	67	0	3	9	79	0.52
#19	40	0	3	9	52	0.34
#20	36	35	2	8	81	0.53

combustion efficiency in the one-dimensional model were decided to show the similar distribution of the calculated wall pressure to that of the measured one.

(8) The impulse function per unit cross section was conserved across the combustion.

(9) The boundary layer was assumed to be turbulent throughout the engine, and the friction coefficient was calculated with the formula of van Driest[8].

(10) The heat flux was calculated with the Reynolds analogy.

4. Results

The operating condition with air flow only is termed the reference condition. The reference condition was expressed as " air " in the figures.

4.1 Effect of strut

Figures 2 (a) to (e) show wall pressure distributions with / without the short strut in the reference condition. In the figures, those of test # 11 are also shown1,2). The fuel flow rate of test #11 is listed in Table 3. In Fig. 2(d), the scale of the wall pressure is different.

The pressure level with the strut was 1.5 times as high as that without the strut around the backward-facing step. On the top wall, the level became higher than that without the strut. It can thus be seen that an increase in pressure was attained by attachment of the strut.

There was a pressure drop just downstream of the backward-facing step. The pressure behind the step seemed to be too high, compared with other results[9]. This was due to the difficulty in measuring very low pressure in the present testing, and also to the effect of the boundary layer. A thick boundary layer suppresses the decrease of pressure behind the step[10]. At $y = 240$ mm, the pressure ratio increased downstream of the step. This was caused by shock wave impingement.

The pressure level near the cowl was very high with or without the strut. The pressure first dropped at the entrance of the isolator, and then increased downstream. The decrease was due to the expansion at the inlet-isolator corner on the side wall, and the increase of the pressure was due to the shock wave from the leading edge of the cowl. The swept angle induces the downward flow toward the cowl, and the open-bottom structure sustains the downward flow. According to the calculated results by the shock wave relation, the air flow turns toward the cowl at 5 degrees at the exit of the inlet. When the air recovers parallel to the cowl surface, the pressure becomes 1.5 times as high as that upstream of the shock wave. In the experiment, around the step, the wall pressure at $y=240$ mm/210 mm was about 1.5 times as high as that at $y=125$ mm and agreed with the above estimation.

According to the one-dimensional calculation, the kinetic energy efficiency of the inlet was estimated to be 0.992, which corresponded to a totalpressure efficiency of 0.88. The kinetic energy efficiency of the present inlet was similar to the empirically estimated value of 0.997 by Waltrup[11].

4.2 Engine operating mode

4.2.1 Visual observation - still photo

Figures 3 (a) to (c) show the still photographs on the typical operating conditions of the model engine. The engine model was mounted upside down, so the cowl was on the top of the model. The fuel flow rates are listed in Table 4.

The operating condition of # 16d was similar to that of the previous testing ; the flame was seen on the top wall side only at the exit of the nozzle[1,2]. According to the photos of # 19e and # 18d, the intensive combustion was attained ; the flame spilled out

Table 3 Fuel flow rate and thrust by FMS

Test No.	Fuel flow rate ($g \cdot s^{-1}$) Normal	Top wall pilot	Side wall pilot	Total	Equivalence ratio Total	Thrust (N)
#11(no strut)	88	2.3	50	140.3	0.94	-900
#16d	26	2.2	8.3	36.5	0.24	-980
#19e	40	2.6	0	42.6	0.28	-250
#18d (unstart)	67	2.9	8.9	78.8	0.53	-1150

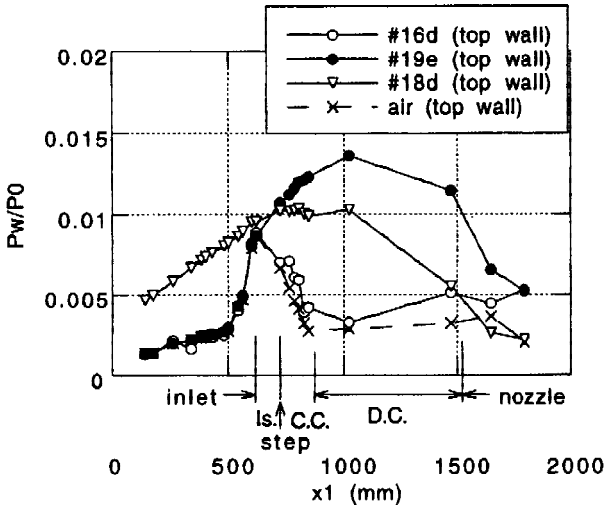

(a) on top wall

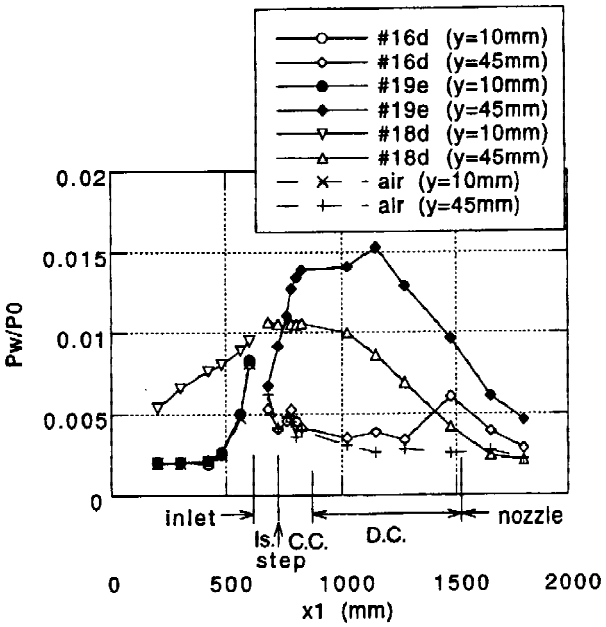

(b) at $y=10$ mm/45 mm

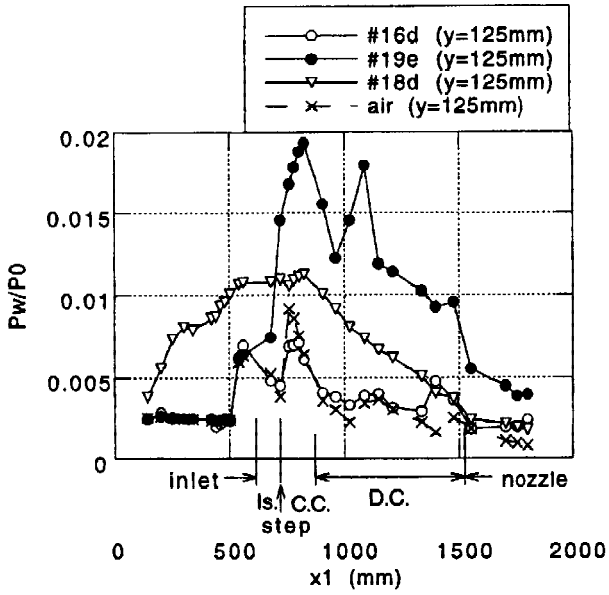

(c) at $y=125$ mm

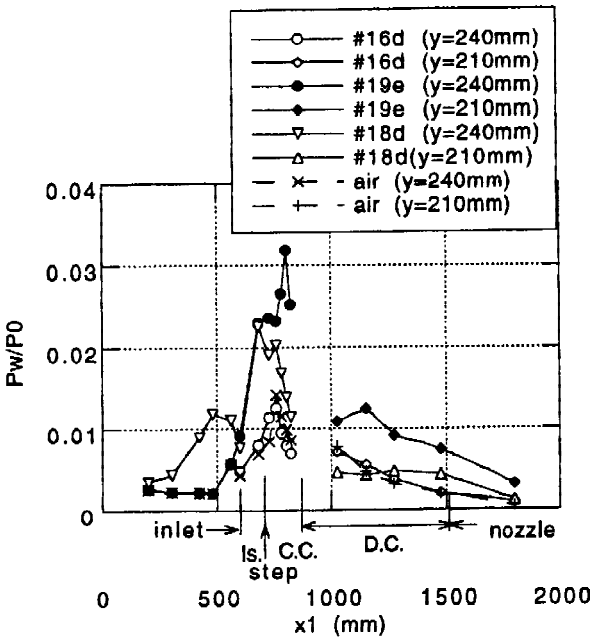

(d) at $y=240$ mm/210 mm

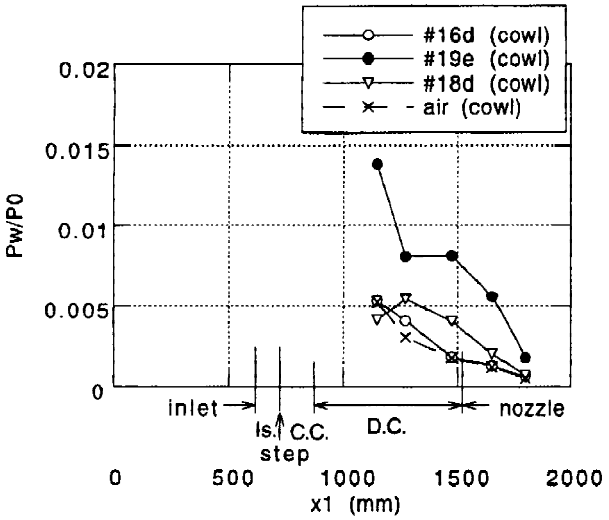

(e) on cowl

Fig. 5 Typical wall pressure distributions

Table 4 Thrust, lift, and pitching moment by FMS

Test No.	Fuel flow rate ($g \cdot s^{-1}$) Total	Thrust (N)	Lift (N)	Pitching moment (N-m)
Air only	-	-1100	300	750
#16d(weak combustion)	36.5	-980	600	500
#19e(intensive combustion)	42.6	-250	-200	1700
#18d(unstart)	78.8	-1150	1500	1450

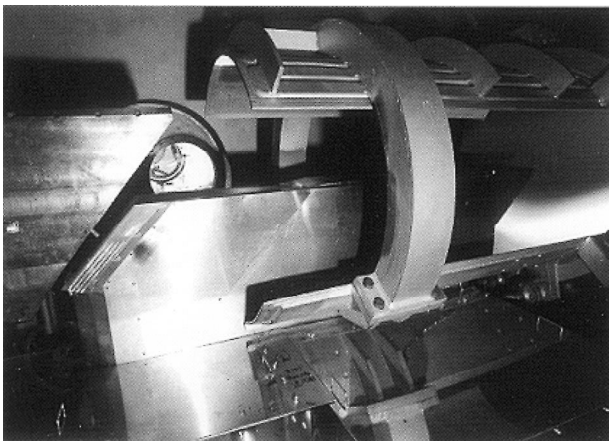

(a) #16d(in start condition with weak combustion)

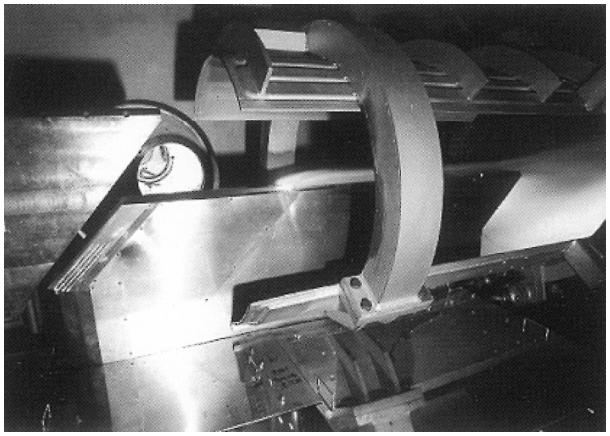

(b) #19e(in start condition with intensive combustion)

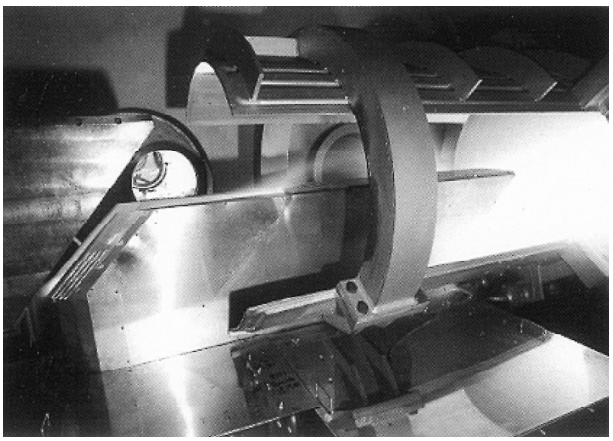

(c) #18d(in unstart condition)

Fig. 3 Engine in operation.

from the leading edge of the cowl in #19e and in #18d. The fuel flow rate of #18d was smaller than that of the previous test, when there was only weak combustion like in #16d [1,2].

4.2.2 Visual observation - schlieren photo

Figures 4 (a) and (b) show the schlieren photos around the bottom of the inlet. In the photos, the air comes from left-hand side, and the black straight edge was the bottom of the inlet. The flow conditions of the reference condition and of #16d were similar to that of #19e, according to the photos, while there was

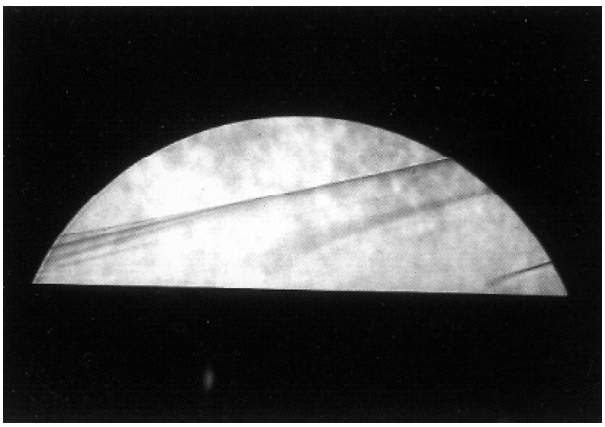

(a) #19e (in start condition)

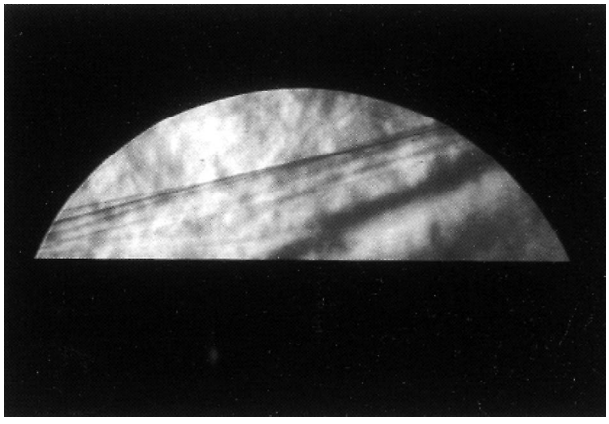

(b) #18d (in unstart condition)

Fig. 4 Schlieren picture around the bottom of the inlet.

separation shock wave from inside of the inlet in the photo of # 18d. Existence of the separation shock from the inlet suggests that the inlet may be in the unstarting condition. Therefore, the model seemed in the starting condition in # 16d and in # 19e, and in the unstarting condition in # 18d.

4.2.3 Wall pressure

Figures 5 (a) to (e) show typical wall pressure distributions. In Fig. 5(d), the scale of the wall pressure is different. In # 16d and # 19e, the wall pressure distributions in the inlet were the same as those of the reference condition ; therefore, the model was in the start condition as was seen in the schlieren pictures.

In # 19e, the level of the wall pressure downstream of the step was much higher than that of the reference condition. The engine was in the intensive-combustion mode. At $y=240$ mm／210 mm and at $y=125$ mm, i.e., far from the top wall, the wall pressure was higher than that of the reference condition even in the isolator. Though there was a pressure drop downstream of the backward facing step at $y=240$ mm, the level of the wall pressure was much higher around the step than that of the reference condition, and the ratio of pressure downstream of the step to that upstream of the step was 1.3 to 1.6, meaning that there was a large, low-velocity region due to combustion behind the step. The large deflection angle on the cowl, which was due to combustion, was estimated to be 22 degrees from the wall pressure distribution at $y=240$ mm.

The shock wave at the step at $y=240$ mm passed $x1=1100$ mm／$y=125$ mm and seemed to impinge at $x1=1500$ mm on the top wall. The second pressure peak around $x1=1100$ mm at $y=125$ mm seemed to be due to the shock wave, but the second peak around $x1=1100$ mm at $y=45$ mm did not correspond to the location of the shock wave exactly. The second peak pressure around $x1=1100$ mm at $y=45$ mm seemed to be due to combustion.

In # 16d, the level of the wall pressure was slightly higher than that of the reference condition in the downstream part of the combustor and in the nozzle, especially around the top wall. The engine was in the weak-combustion mode. Though there was a pressure increase behind the step at $y=240$ mm, the high-pressure region behind the step was short, and the pressure level was more similar to that of the reference condition than to that of # 19e. There was no intensive heat release behind the step. According to the one-dimensional calculation, the combustion efficiency of # 19e was 95%, while the efficiency of # 16d was only 2%.

In # 18d, the mean pressure distribution in the inlet was different from that of the reference condition, and the engine model was in the unstart condition. The pressure distribution on the top wall was similar to that on the side wall except at $y=240$ mm, and the level of the pressure was high. Near the cowl, the level of the wall pressure was not high, and it was similar to that of the reference condition. The deflection angle on the cowl becomes large because of the large flow-deflection toward the cowl in the inlet caused by the separation on the top wall, and there is a strong shock wave from the leading edge of the cowl. According to the pressure distribution in the inlet, the pressure ratio across the separation shock wave was 5, and the Mach number behind the shock wave was 3.6, respectively. The effect of the separation shock wave encompassed most of the inlet. Though the pressure was high in the inlet, it was much lower than the pressure after the normal shock wave. It would have been non-dimensionalized pressure of 0.04, if the normal shock had existed at the entrance of the inlet.

4.2.4 Heat flux

Figures 6 (a) to (c) show the heat flux distributions. In the reference condition, the heat fluxes were roughly uniform.

When the engine was in the intensive-combustion mode as in # 19e, the level of the heat flux was high in the combustor and in the nozzle. The heat flux can increase upstream of combustion due to the increase of the heat transfer coefficient, but the effect of adiabatic wall temperature on heat flux is much greater than that of the heat transfer coefficient. The large heat flux indicates the location of combustion gas. On the top wall, the location of the first peak heat flux agreed with the step position. The wall pressure gradually increased, but the heat flux first decreased downstream of the first peak, then increased. The location of the second peak agreed with that of the second peak of the wall pressure. Because there was no impingement of a strong shock wave there, the large heat flux was due to heat release, and the primary heat release

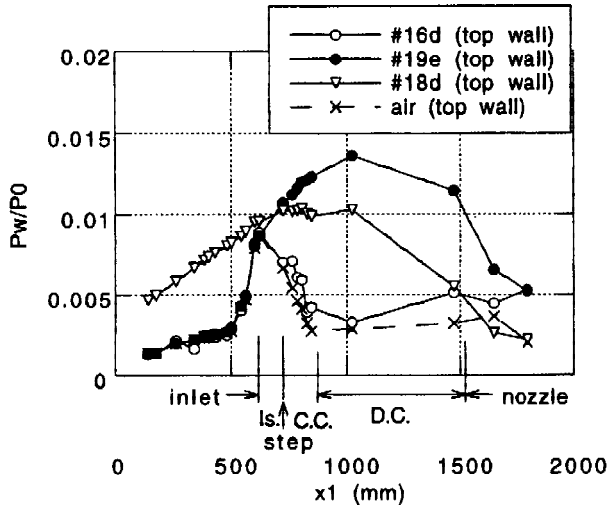

(a) on top wall

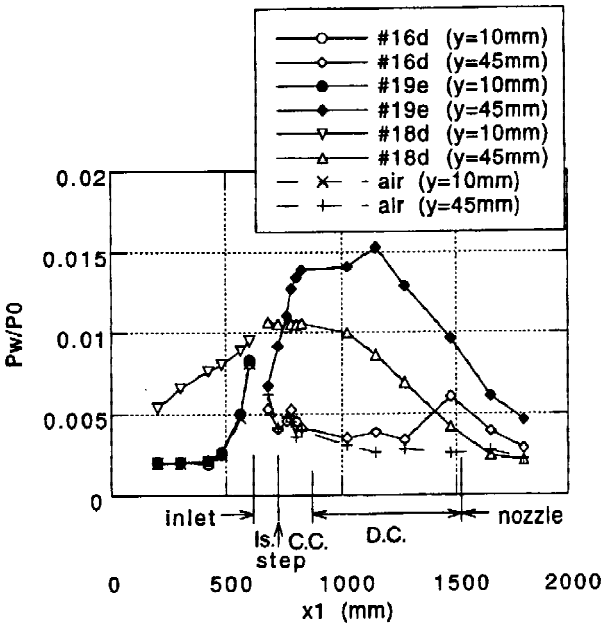

(b) at $y=10$ mm/45 mm

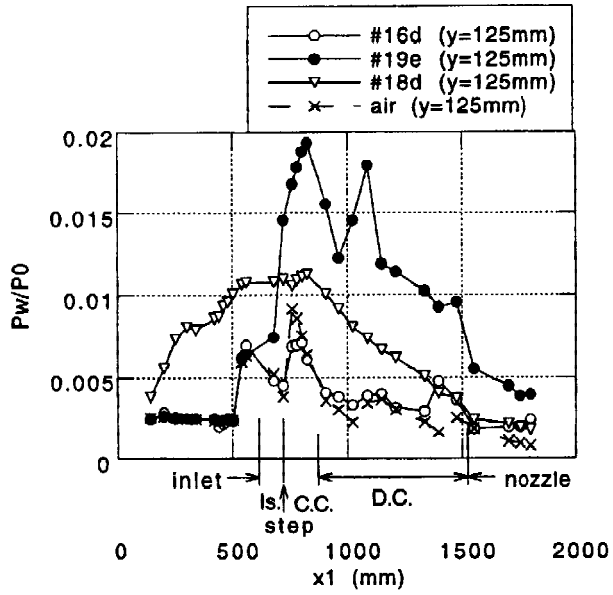

(c) at $y=125$ mm

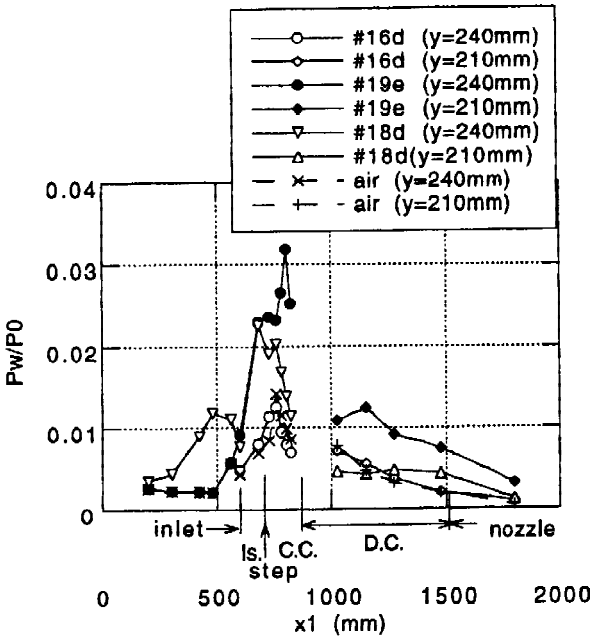

(d) at $y=240$ mm/210 mm

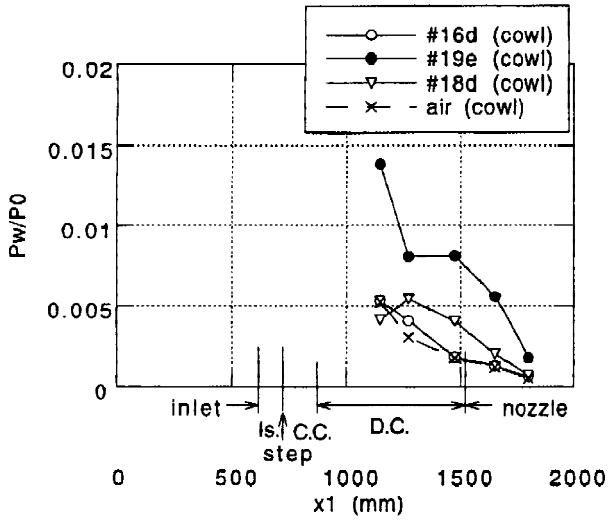

(e) on cowl

Fig. 5 Typical wall pressure distributions

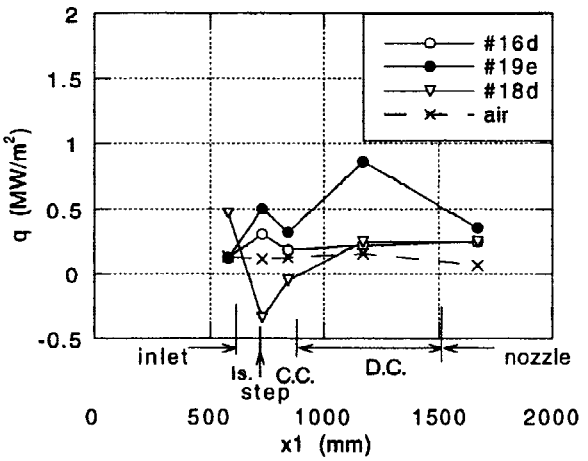

(a) on top wall

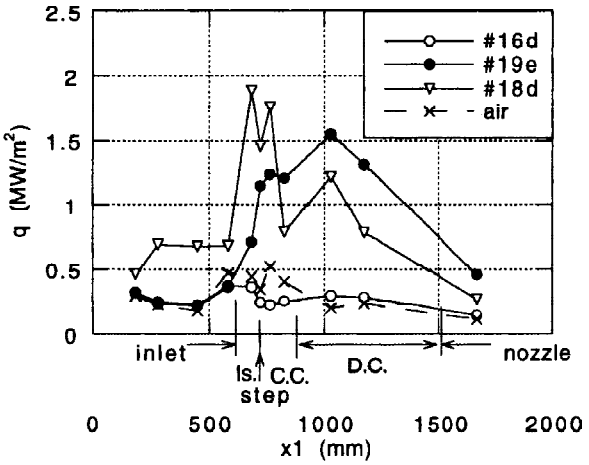

(b) at y=125 mm

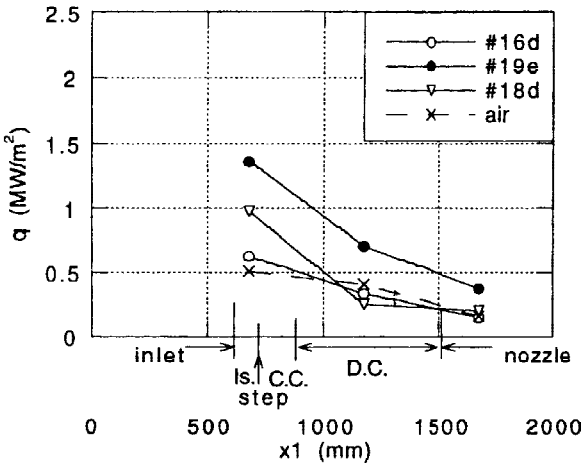

(c) on cowl

Fig. 6 Typical heat flux distributions

occurred in the divergent part of the combustor on the top wall. On the top wall, there were no primary fuel injection ports, so fuel had to travel some distance from the side wall to the top wall.

On the side wall, there was a shoulder point at the step, and there was a peak point in the divergent part of the combustor. At y = 125 mm, the second peak pressure at $x1$=1100 mm was similar to the first one at $x1$=800 mm, while the peak heat flux at $x1$=1000 mm was higher than the flux at $x1$=800 mm. According to the one-dimensional calculation of the intensive-combustion mode, the heat flux from the combustion gas was 2.2 MW·m^{-2}, and that from the residual air was 0.7 MW·m^{-2} on the side wall of the constant duct part of the combustor. The level of the measured heat flux on the side wall was similar to that due to the combustion gas in the one-dimensional calculation.

In the weak-combustion mode of #16d, the heat flux distribution on the top wall was slightly larger than that of the reference condition in the nozzle. It agreed with the wall pressure distribution of Fig. 5(a). There was a small peak of heat flux around the step on the top wall, and such a peak was also observed in #19e. It seemed to be due to the pilot fuel combustion by the plasma ignitors. On the side wall, the heat flux level was lower around the step than that of the reference condition. The flame did not propagate from the top wall to the side wall behind the step.

In the unstart condition of #18d, the top wall was cooled around the step, and the heat flux distribution resembled that of the reference condition downstream of the combustor on the top wall, while the heat fluxes were high around the step on the side wall. On the cowl, the level was near that of the reference condition, as well as the level of the wall pressure. In the inlet, the level of the heat flux was about four times as high as that of the reference condition. The wall pressure in Fig. 5(c) was also about four times as high as that of the reference condition. The increase of heat flux in the inlet in the unstart condition was due to the increase of the pressure level, i.e., an increase of the heat transfer coefficient.

4.2.5 Force and moment

Figure 7(a) shows the engine thrust measured by FMS. The designations' FMS 'and' W.P. 'in the figures indicate the value measured by FMS and the value due to the integration of the wall pressure, respectively. The integration of the wall pressure did not include the pressure on the strut. ' N + T ' and ' T ' represent a combination of normal injection and tangential injection of fuel, and tangential injection, respectively. The results for tangential injection are mentioned later. Table 4 lists thrust, lift, and pitching moment of typical operating conditions.

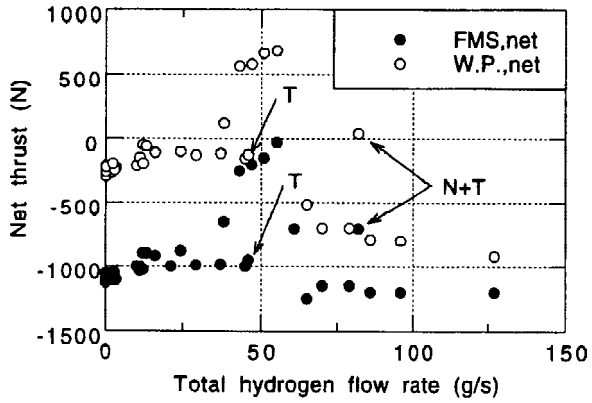

(a) Thrust

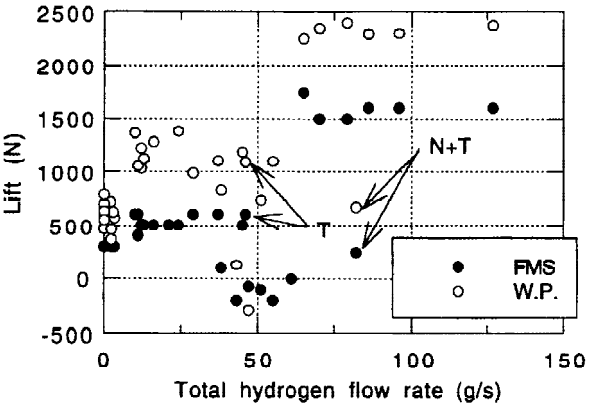

(b) Lift

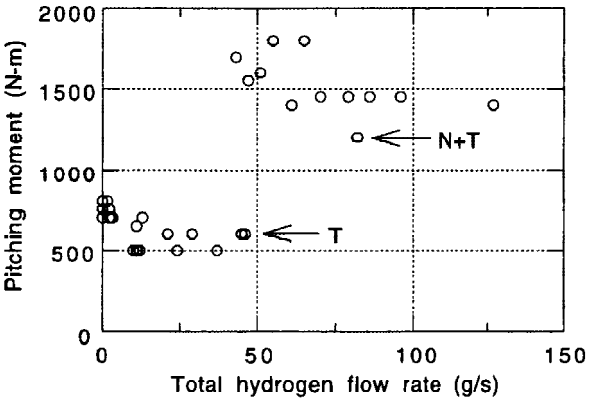

(c) Pitching moment

Fig. 7 Force and moment

Discrete changes in thrust level can be seen in Fig. 7(a). The thrust was large in the intensive-combustion mode in the narrow range of the fuel flow rate of about 50 $g \cdot s^{-1}$. There were two thrust levels for a fuel flow rate of 40 $g \cdot s^{-1}$, mentioned later in Section 4.4.2. When the fuel flow rate was greater than 60 $g \cdot s^{-1}$, the engine was in the unstart condition. The unstart condition induced more drag than the reference condition. As shown in Fig. 5, this was due to the high pressure level in the inlet and the moderate pressure level downstream of the combustor. According to the wall pressure integration, the drag in the inlet was 1140 N in the unstart condition of # 18d, while it was 490 N in the start condition of # 19e. According to the one dimensional calculation results, the friction drag and pressure drag acting outside of the side wall were estimated to be 260 N. The net, positive engine thrust was estimated by compensating the drag acting outside of the side wall for the measured thrust by FMS in the intensive-combustion mode.

Figure 7(b) shows the lift. In the intensive-combustion mode, the lift was negative. The pressure around the cowl was very high in the vicinity of the step, indicating that the large force on the cowl canceled the lifting force in the inlet. In the weak-combustion mode, there was weak combustion around the top wall in the divergent part of the combustor, so the lift was slightly larger than that of the reference condition. In the unstart condition, the lift became very large due to the high pressure in the inlet.

Figure 7(c) shows the pitching moment measured by FMS. The pitching moment was positive in every test, even in the reference condition. This was due to the high pressure at the step near the cowl and the bottomless shape of the inlet. In the intensive-combustion mode, the large force acted on the cowl in the y-direction, and thus the pitching moment became large. In the unstart condition, the pitching moment was also large due to the high pressure level in the inlet. In the weak-combustion mode, the pressure on the top wall was slightly larger than that of the reference condition in the divergent part of the combustor

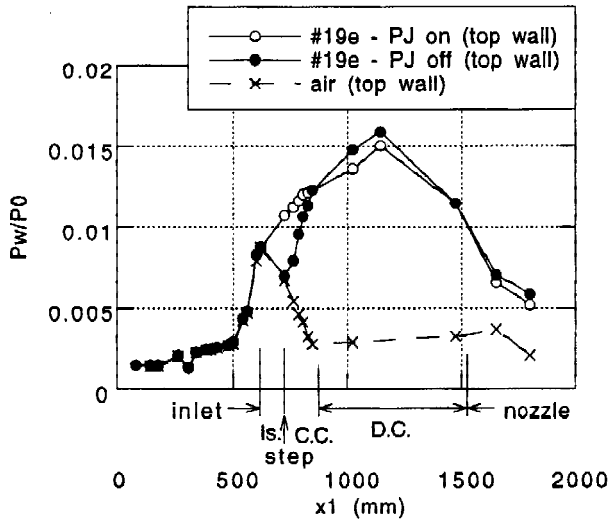

(a) on top wall

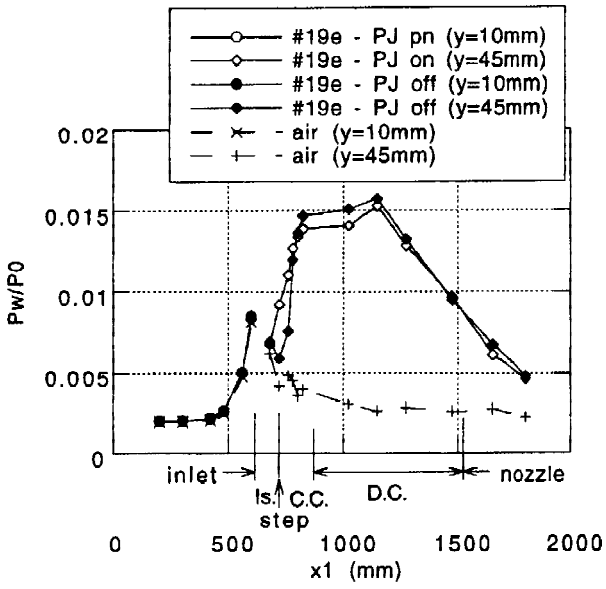

(b) at $y=10$ mm/45 mm

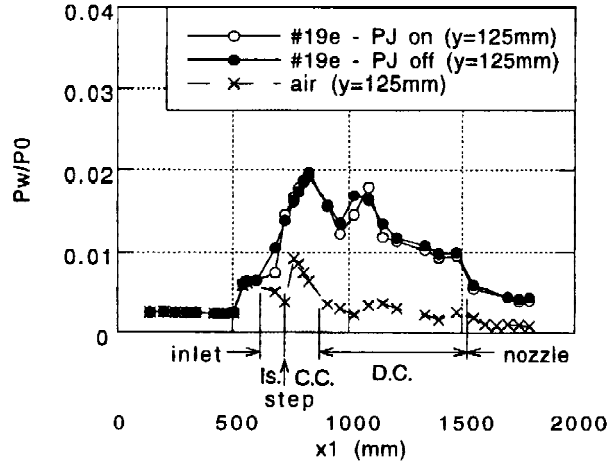

(c) at $y=125$ mm

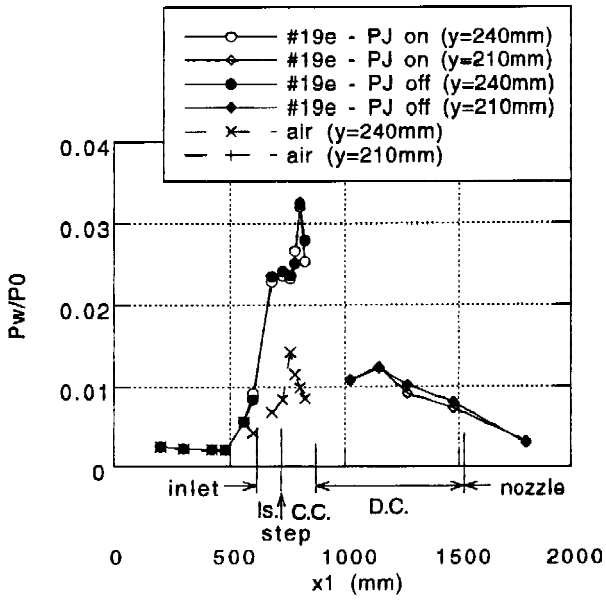

(d) at $y=240$ mm/210 mm

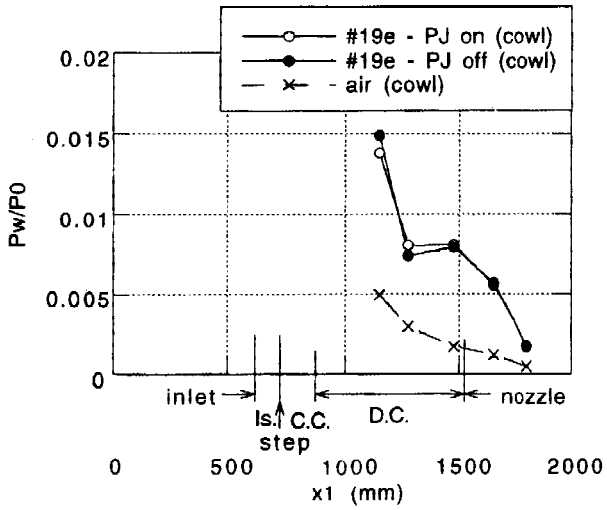

(e) on cowl

Fig. 8 Wall pressure distributions - effect of plasma ignitor

and in the nozzle, so the pitching moment was slightly smaller than that measured in the reference condition.

4. 3 Effect of plasma ignitor／flame holders

Figures 8 (a) to (e) show the wall pressure distributions, and Figures 9 (a) to (e) show the heat flux distribution. First, the model was in the operating condition of #19e with the operation of the plasma ignitors／flame holders (PJ on). Then, the ignitors／holders were turned off with no change of the fuel flow rates (PJ off). The pressure level on the top wall and at $y = 10$ mm／45 mm decreased around the plasma ignitors／flame holders after the turning-off of the ignitors／holders. On the other hand, the level did not change at $y = 125$ mm, at $y = 240$ mm／210 mm and on the cowl. The heat fluxes on the top wall also greatly decreased around the ignitors／holders after the plasma ignitors were turned off. After the plasma ignitors／flame holders were turned off, the heat fluxes on the side wall near the top wall were slightly smaller than those with operation of the plasma ignitors. Around the cowl, there was no change.

Once intensive combustion was attained, the effect of the plasma ignitors was limited in their vicinity and the flame was held irrespective of the plasma ignitors.

4. 4 Intensive combustion

4.4.1 Effect of fuel flow rate

There were four operations of the intensive-combustion mode in the present testing. The fuel flow rates and the thrust are listed in Table 5. Figures 10(a) to (e) show wall pressure distributions of #19e and #14e. Within the intensive-combustion mode, the fuel flow rate was smallest in #19e and largest in #14e.

The level of the wall pressure in the combustor increased with the fuel flow rate. The heat release seemed to increase with the fuel flow rate. The pressure distributions in the isolator on the top wall and at $y = 10$ mm／45 mm were similar to those of the

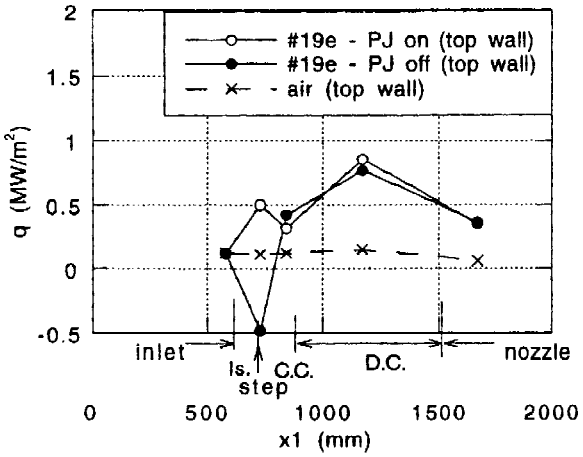

(a) on top wall

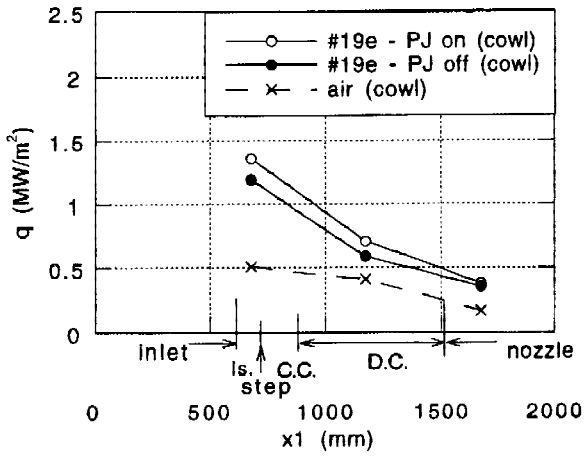

(e) on cowl

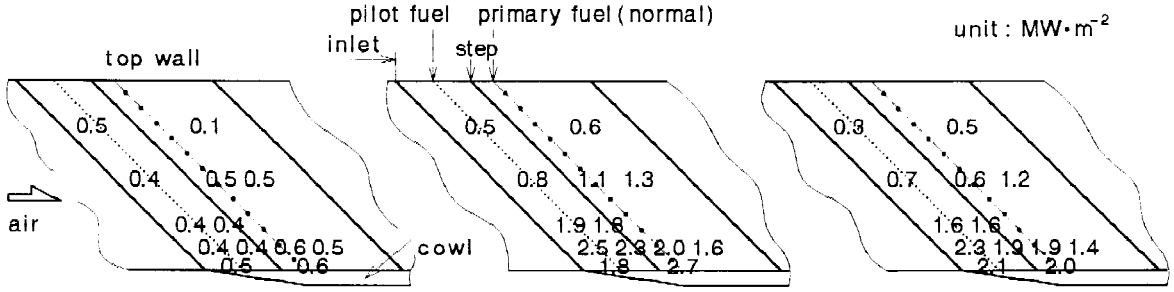

(b) Air flow (reference condition)

(c) #19e (intensive combustion, ignitors-on)

(d) #19e (intensive combustion, ignitors-off)

Fig. 9 Heat flux distributions - effect of plasma ignitor

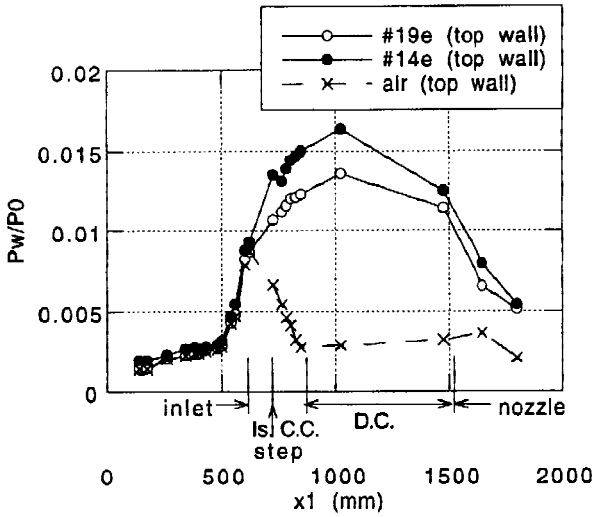

(a) on top wall

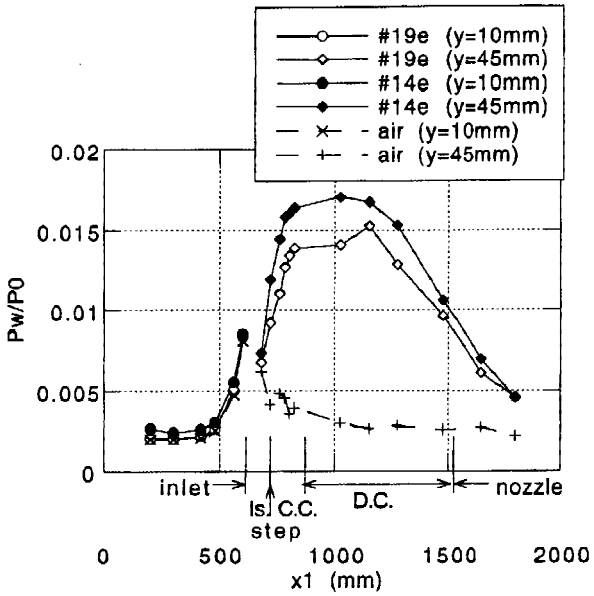

(b) at $y=10$ mm/45 mm

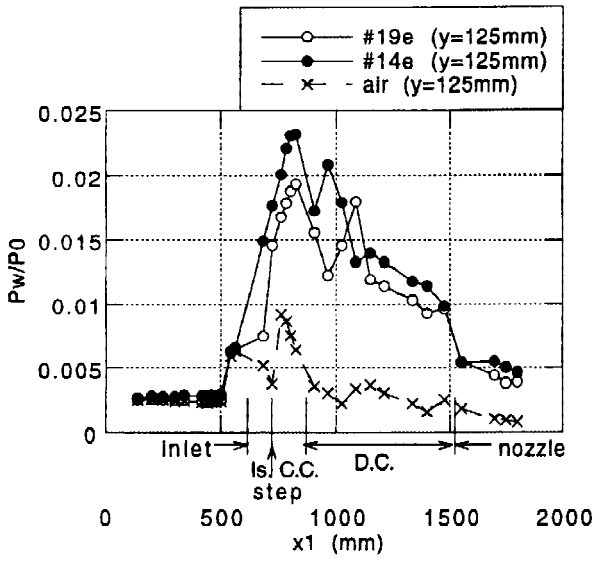

(c) at $y=125$ mm

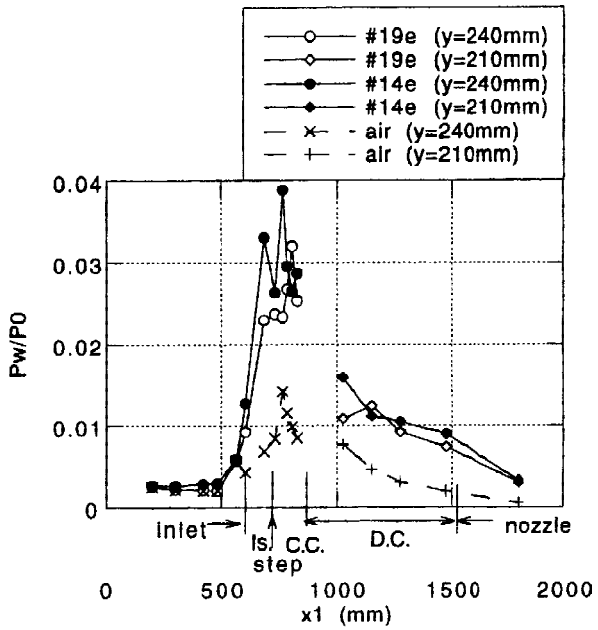

(d) at $y=240$ mm/210 mm

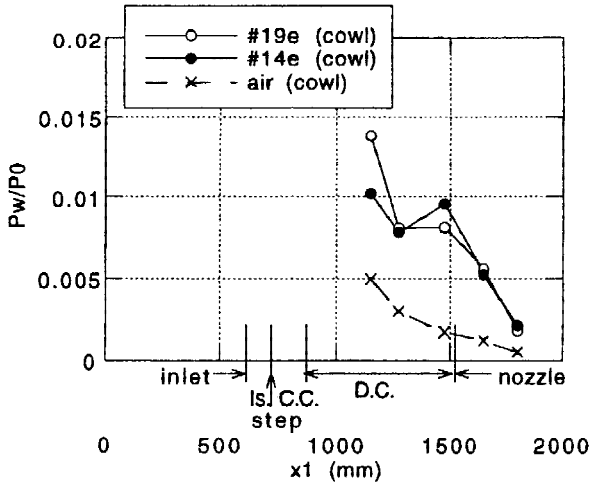

(e) on cowl

Fig. 10 Wall pressure distribution in intensive-combustion mode

Table 5 Fuel flow rate and thrust by FMS in the intensive-combustion mode

Test No.	Fuel flow rate ($g \cdot s^{-1}$)				Equivalence ratio	Thrust (N)
	Normal	Top wall pilot	Side wall pilot	Total	Total	
#19e	40	2.6	0	42.6	0.28	-250
#20d	36	2.3	8.4	46.7	0.31	-200
#19d	40	2.6	8.8	51.4	0.34	-150
#14c	53	2.3	0	55.3	0.37	-30

reference condition. The level of the side wall pressure at $y = 240$ mm／210 mm was very high around the step. The levels at $y = 125$ mm and $y = 240$ mm／210 mm were already higher than those of the reference condition in the isolator.

Figures 11 (a) to (c) show the heat flux distributions. On the top wall, there were two peaks around the step and in the divergent part of the combustor. The level of the heat flux around the step increased with the fuel flow rate. On the other hand, the flux in the combustor decreased in the # 14e, in which the fuel flow rate was largest in the four tests. On the side wall, the level of the heat flux increased from the isolator to the upstream section of the combustor, and decreased in the downstream with the fuel flow rate. The decrease of the heat flux in the downstream sec-

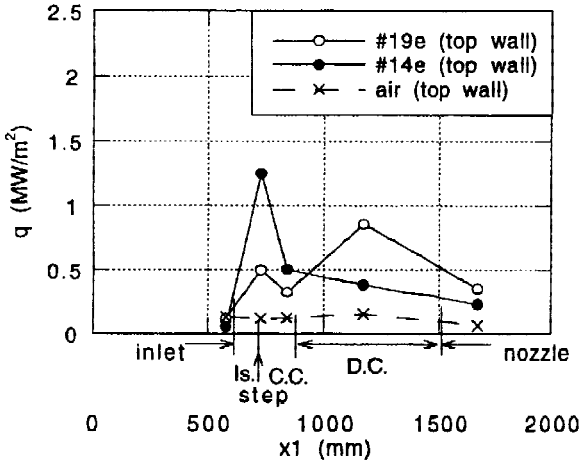

(a) on top wall

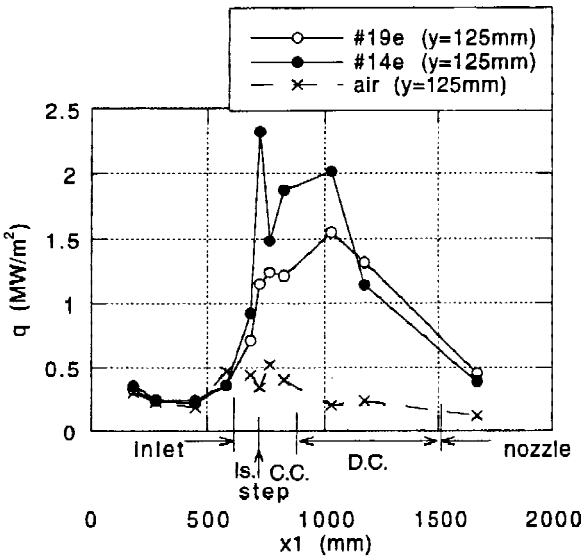

(b) at $y = 125$ mm

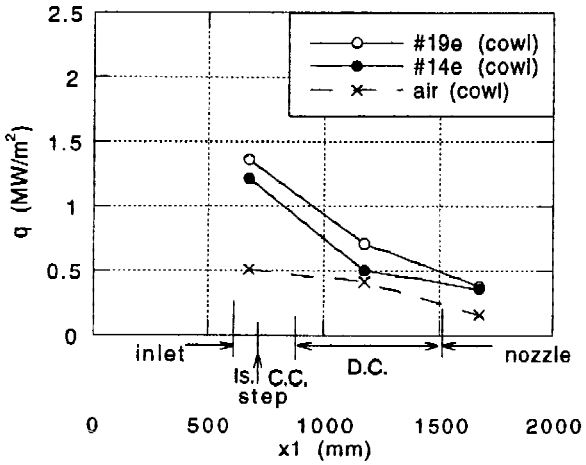

(c) on cowl

Fig. 11 Heat flux distributions in intensive-combustion mode

tion of the combustor did not correspond to the change of the wall pressure, which increased with the fuel flow rate. When the fuel flow rate was large, the position of the heat release seemed to move upstream with the fuel flow rate.

4.4.2 Effects of fuel injection method

In test #20, as shown in Table 6, the usage of only the normal injection of the primary fuel was not able to attain intensive combustion in #20c. The addition of the side wall pilot fuel resulted in the intensive combustion in #20d. The concentration of the fuel or the total fuel flow rate also seemed to be important in the vicinity of the step.

On the other hand, in the present testing, the intensive combustion in # 19e and # 20d and the weak combustion in #12c were observed at the same total fuel flow rate of around 45 $g \cdot s^{-1}$ as shown in Table 6 and Figures 12 (a) to (c). Almost all the fuel was

Table 6 Fuel flow rate and thrust by FMS

Test No.	Fuel flow rate ($g \cdot s^{-1}$)				Equivalence ratio	Thrust (N)
	Normal	Top wall pilot	Side wall pilot	Total	Total	
#20c	36	2.3	0	38.3	0.26	-650
#20d	36	2.3	8.4	46.7	0.31	-200
#19e	40	2.6	0	42.6	0.28	-250
#12c	0	3.1	42	45.1	0.30	-1000

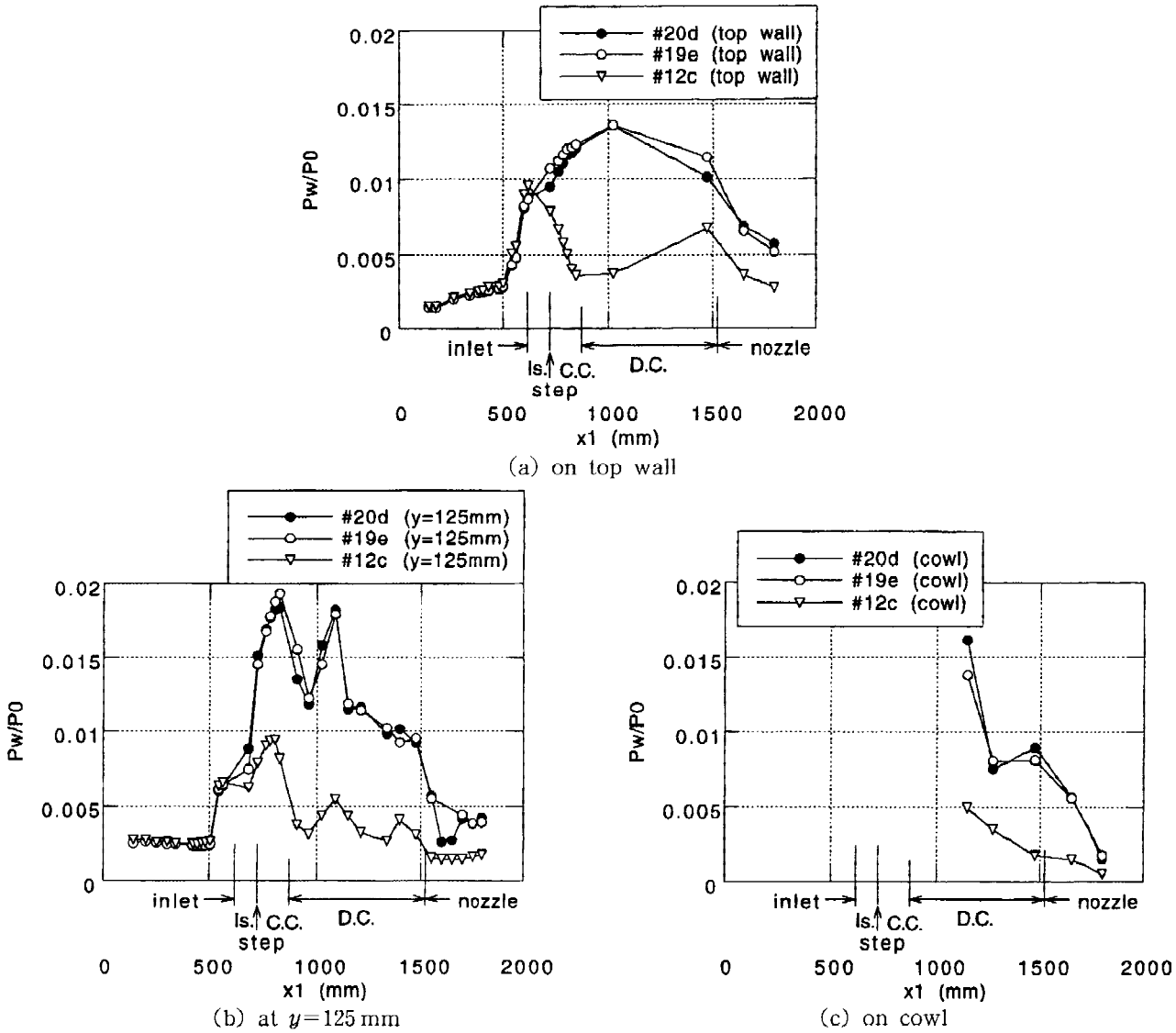

(a) on top wall

(b) at $y=125$ mm

(c) on cowl

Fig. 12 Wall pressure distributions - effect of fuel injection method

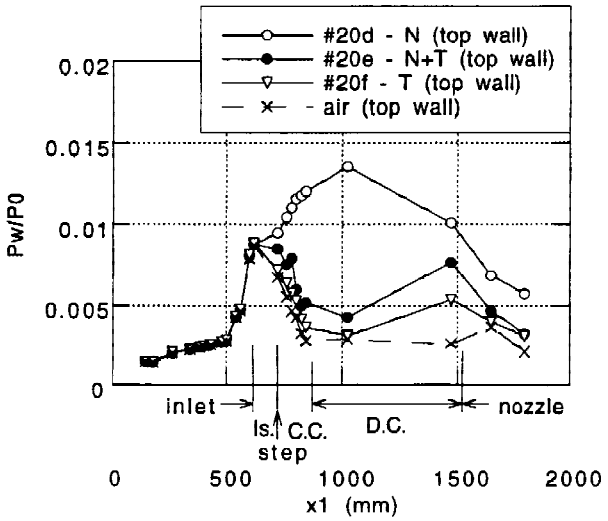

(a) on top wall

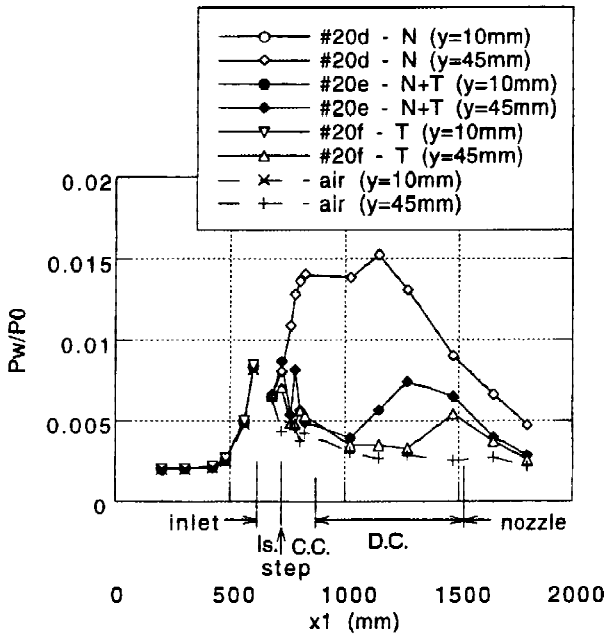

(b) at y=10 mm/45 mm

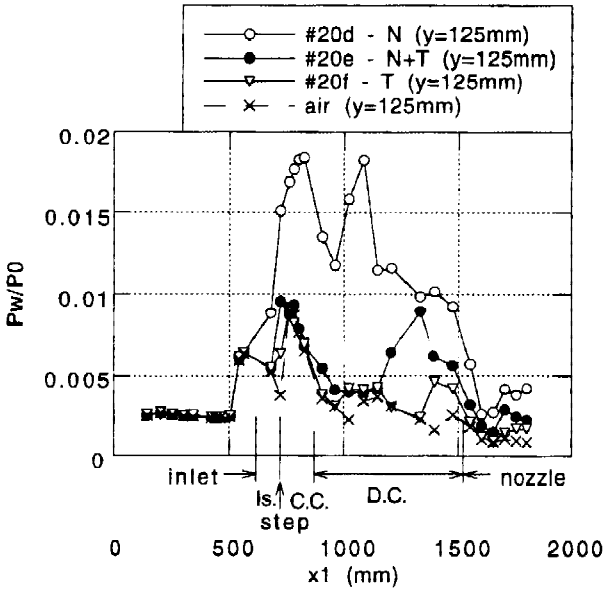

(c) at y=125 mm

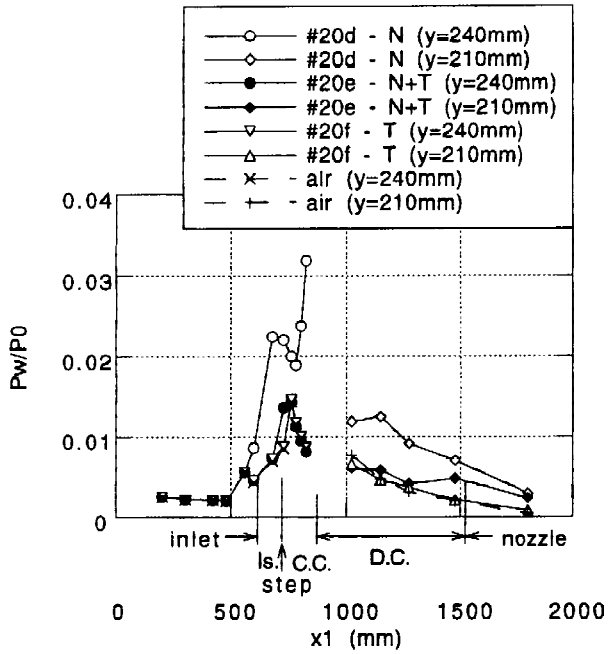

(d) at y=240 mm/210 mm

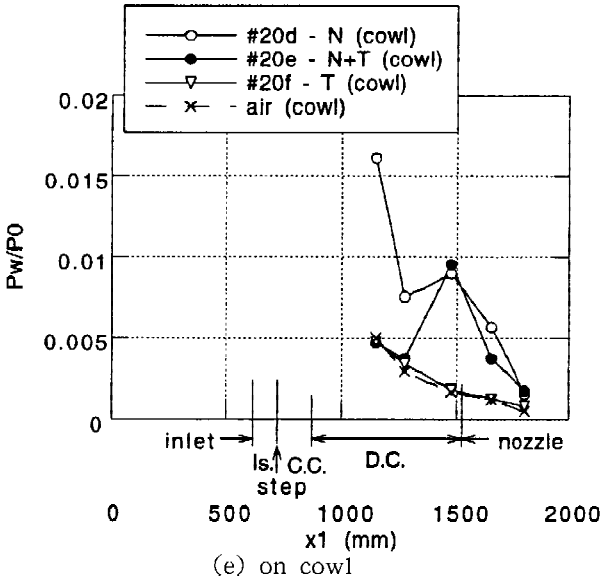

(e) on cowl

Fig. 13 Wall pressure distributions - effect of tangential injection

Table 7 Fuel flow rate and thrust by FMS

Test No.	Fuel flow rate ($g \cdot s^{-1}$)					Equivalence ratio	Thrust (N)
	Normal	Tangential	Top wall pilot	Side wall pilot	Total	Total	
#20d	36	0	2.3	8.4	46.7	0.31	-200
#20e	36	35	2.3	8.4	81.7	0.54	-700
#20f	0	35	2.3	8.4	45.7	0.30	-950

injected downstream of the step in #19e and #20d, while it was injected upstream of the step in # 12c. Though the concentration of the fuel around the step was important, the normal fuel injection downstream of the step was indispensable for attaining intensive combustion.

In the present testing, tangential fuel injection was investigated in only one test, i.e., #20. The fuel flow rate rates are listed in Table 7. The thrust decreased with the tangential injection of fuel as shown in Fig. 6 and Table 7. The thrust produced by the tangential, unburned gas injection was about 100 N in # 20e and # 20f. The decrease of drag in # 20f was mainly due to the gas injection. Figures 13 (a) to (e) show the wall pressure distributions, and Figures 14 (a) to (c) show the heat flux distributions. The wall pressure distributions and the heat flux distributions with the tangential injection were almost the same as those of #16d in the weak-combustion mode. When the normal fuel injection was also used with the tangential injection in # 20e, the level of the pressure was higher in the combustor than when only the tan-

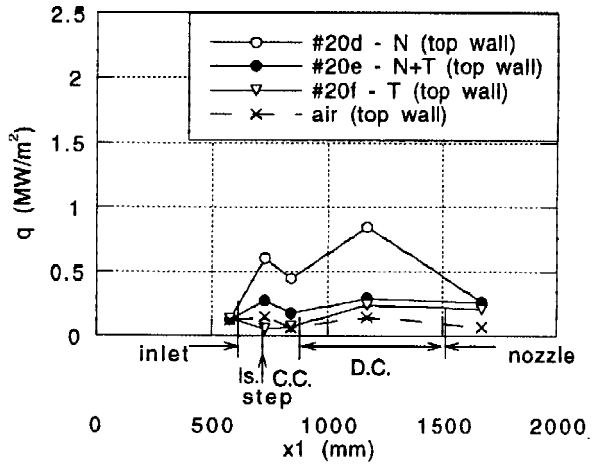

(a) on top wall

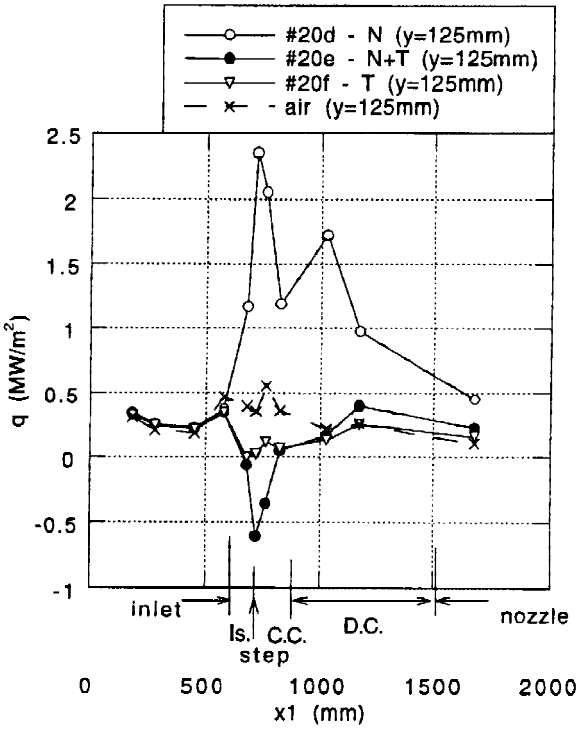

(b) at $y=125$ mm

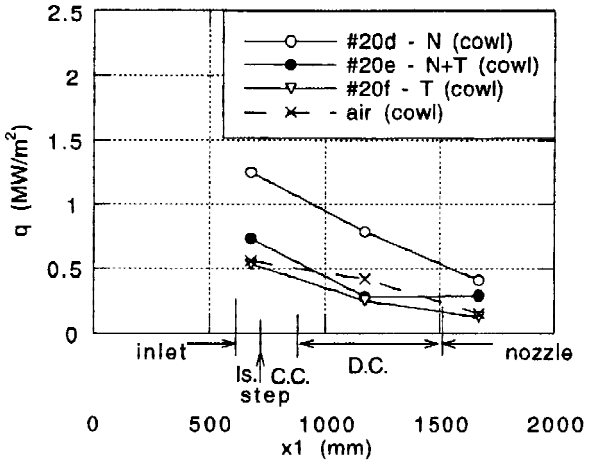

(c) on cowl

Fig. 14 Heat flux distribution - effect of tangential injection

Table 8 Fuel flow rate and thrust by FMS

Test No.	Fuel flow rate ($g \cdot s^{-1}$) Normal	Top wall pilot	Side wall pilot	Total	Equivalence ratio Total	Thrust (N)
#14d	53	2.3	9.7	65.0	0.43	-1250
#14e	53	2.3	0	55.3	0.37	-30

gential fuel injection was used in #20f.

There was not large difference in the heat flux distributions on the side wall of #20e from that of #20f except around the step. Around the step on the side wall, the heat flux level of #20e was negative. It seemed to be abrupt decrease of the wall temperature from the intensive-combustion mode (#20d) to the weak- combustion mode (#20e). On the top wall, the heat flux level of #20e, in which there were both the normal injection and the tangential injection, was slightly larger around the step than that of #20f, in which there was only the tangential injection.

4.5 Re - start

In test #14, the engine moved from the unstart condition of #14d to the start condition of #14e when the injection of the side wall pilot fuel of $9.7 g \cdot s^{-1}$ was stopped (Table 8). There was no difficulty in changing from the unstart to the start condition.

5. Discussion

5.1 Intensive combustion

The mechanism of the intensive combustion, which produced thrust, is discussed first. Intensive combustion was attained with the following conditions : (1) usage of a short strut, (2) normal fuel injection downstream of the step, and (3) a suitable fuel flow rate.

5.1.1 Role of strut

As shown in Fig. 2 (a) to (e), when a large amount of fuel was injected normally in the model with no strut as in #11, there was no pressure drop at the step, and the pressure level was similar to or higher than that of the reference condition with the strut on the side wall. However, the pressure level on the top wall around the step was low even with such a high fuel flow rate in the model with no strut, and the level was 0.5 times as low as that of the reference condition with the strut. A pressure increase around the step was attained by (1) the usage of a strut around the fuel injector. According to results of the inlet testing with the strut, there was a large, disturbed, low-velocity region around the foot of the strut [12]. Such a region with high pressure was necessary for the initiation of intensive combustion. However, the conditions were not sufficient to attain intensive combustion, because there was a weak-combustion mode even with the strut.

5.1.2 Low velocity region behind the step

In the design procedure of the original engine model which had a strut [2], the length from the step to the fuel injector of 20 mm, which was five times as large as the height of the step, was determined so as to avoid interaction between the separated boundary layer and the fuel injected behind the reattachment of the boundary layer [13,14]. The re-circulation region behind the step was designed to be used for flame holding of the pilot fuel. The avoidance of the interaction seemed to be necessary for preventing the gas behind the step from reaching an overly dense fuel condition and becoming too cool.

Conditions (2) and (3) created a high-pressure, low-velocity region between the backward-facing step and the normal fuel injection holes on the side wall by the interaction between the boundary layer and the injected fuel [15]. The designed configuration of the step-injector location was not suitable for the Mach 6 operation. Creation of the interaction was insufficient, because there was a low-velocity region even in the weak-combustion mode and in the engine with no strut, as shown in Figs. 2. The location and the size of the low-velocity region are important.

The flame probably propagated in the low-velocity region from the top wall to the cowl in the intensive-combustion mode. In the weak-combustion mode, there was a pressure drop at the step on the side wall at $y = 10$ mm／45 mm ; this means that there was no large, low-velocity region behind the step there. Thus, the flame did not propagate to the cowl. Once the flame was propagated near the cowl, a large, low-velocity region was created there by combustion, and the flame was sustained, even after the plasma ignitors were

turned off.

5.1.3 Possibility of a large, low-velocity region

To examine the possibility of the existence of a large, low-velocity region at the step, the locations of the center of the Mach disk in the normally injected fuel jet and the diameters of the fuel jet at the Mach disk position without chemical reaction were calculated with the model by Billig et al. [16], the results being shown in Table 9. The coordinates of the Mach disk location were distance from the injection hole and the height from the wall surface. To estimate the upstream or y-direction propagation of the downstream flow structure change, the detachment length of the shock wave caused by the injected fuel was also calculated with the Billig's model [17]. The fuel jet was assumed to be a cylinder with the diameter of the fuel jet at the Mach disk position. The calculated diameter is also shown in Table 9. In the calculation, the Mach number and other properties of the primary flow were those of the one-dimensional calculation.

According to the calculated results, the penetration lengths, the detachment lengths, and the fuel jet diameters were very small. There must be no interaction between the boundary layer and the injected fuel on the side wall in such flow conditions as those listed in Table 9.

The boundary layer thickness of 99% velocity was 58 mm at the entrance of the engine model [3], and the fuel injection port nearest the top wall, located at $y=$ 5 mm, seemed to be in the boundary layer. Moreover, when there was a strut, a low velocity region was created around its foot [12]. Therefore, the injection port was in the low velocity region. When the fuel is injected into a low Mach number flow, the detachment length, the diameter of the fuel jet, and the difference of the detachment length due to the fuel flow rate all increase. For example, when the Mach number at the injection port is 1.4, the detachment lengths of the intensive-combustion mode and the weak-combustion mode are 9 mm and 7 mm, respectively. The diameters of the fuel jet of the combustion modes are 4.5 mm and 3.5 mm, respectively, and the difference of the lengths and the diameters are enlarged. Meanwhile, the reattachment length of the boundary layer over the backward-facing step increases with the thickness of the incoming boundary layer [10], i.e., with growth of the low-velocity region. The attachment of the strut caused the interaction between the fuel injection and the reattaching boundary layer, and the interaction created a large, low-velocity region between the step and the fuel injection port. The interaction also spread in the y-direction on the side wall near the top wall.

The tangential injection blew off the low-velocity region around the step, and the flame was no longer anchored. The operating mode thus changed to the weak-combustion mode. Tangential injection with the present fuel flow rates was not suitable for the present engine configuration or for the present engine operating conditions.

5.1.4 Combustion efficiency

In the intensive-combustion mode, there was probably a wide, low-velocity region around the step, especially around the cowl. Mixing and combustion probably occurred around the low-velocity region, and this resulted in the high combustion efficiency.

In the weak-combustion mode, the pilot fuel flow rate from the top wall was about 6 % of the total fuel flow rate, and the value was similar to that of the estimated combustion efficiency of 2 %. Therefore, most of the combusted fuel seemed to be the pilot fuel injected from the top wall. There was no large, low-velocity region on the side wall in the weak-combustion mode, and there was no residence time for mixing and reaction around the step. Furthermore, there was no ignition source on the side wall. The combustion observed in the nozzle in the weak-combustion mode was due to self-ignition after supersonic mixing.

Table 9 Normally injected fuel jet geometry without chemical reaction (unit: mm)

Fuel flow rate per injection port ($g \cdot s^{-1}$)	Mach No.	Mach disk location (distance, height)	Fuel jet diameter at Mach disk	Detachment length
2.8(No strut)	4.0	(2.8, 2.3)	2.2	0.6
2.1(Strut, intensive-combustion mode)	3.6	(2.3, 1.9)	1.9	0.5
1.3(Strut, weak-combustion mode)	3.6	(1.8, 1.5)	1.5	0.4

5.2 Unstart condition

5.2.1 Initiation of unstart

In Mach 4 testing of inlets [18] and in the Mach 4 testing in the RJTF [1,2], gradual transition from the start condition to the unstart condition was observed; it clearly appeared in the top-wall pressure distribution. In the present Mach 6 testing, such gradual transition was not observed.

When the swept angle was small, the change from the start to the unstart condition abruptly occurred in the Mach 4 flow condition [18]. In the present testing, the inflow Mach number of 5.3 was higher than 4, and the effect of the swept angle became smaller than that in the Mach 4 flow condition. Therefore, the high Mach number was probably one of the reasons of the abrupt change of the inlet condition.

The wall pressure in the isolator at $y = 10$ mm／45 mm did not change with the increase of the fuel flow rate in the intensive-combustion mode, while that at $y = 240$ mm／210mm greatly increased with the fuel flow rate. In the region with increased pressure, there was a thick, low-velocity region on the wall. Therefore, the low-velocity region seemed to grow from the cowl with the increase of the fuel flow rate, and the low-velocity region seemed to reduce the substantial cross section, and／or to interact with the boundary layer on the side wall to induce the large separation.

The length of the isolator was designed to avoid the inlet-combustor interaction in the lowest Mach number condition at the RJTF, i.e., the Mach 4 flight condition, in which the pressure increase was anticipated to reach the most upstream point in the isolator[19-22]. As planned in the design procedure, in the present Mach 6 testing, the large pressure increase in the isolator was not observed in the start condition except around the cowl. In the designing procedure, the strong, inlet-isolator-cowl interaction enhanced by the combustion, which appeared in the present testing, was unforeseeable. One of the reasons for the narrow region of the start condition was the interaction around the cowl. To enlarge the start condition with greater fuel flow rates, several improvements are possible, e.g., elongation of the isolator, change of the combustor configuration, and suitable distribution of the injected fuel. Elongation of the isolator and change of the combustor are under investiga-tion [23,24].

5.2.2 Re - start

In test # 14, the engine condition suddenly changed from the unstart to the start condition due to reduction of the fuel flow rate. Good re-startability is apparently due to the swept angle and the open-bottom structure of the inlet. When there is a swept angle, the leading edge of the cowl is located far downstream of the exit of the inlet on the top wall. Therefore, the substantial open area of the inlet is wide with the swept angle, and the excess fluid can spill out easily in the unstart condition. The adoption of the swept angle and the open-bottom structure will be necessary for design of scramjet engines. For a ramp-compression type inlet, a substitute mechanism for the swept angle and the open-bottom structure is necessary for good startability.

6. Concluding Remarks

A sub-scale scramjet engine model with a short strut was tested under Mach 6 flight conditions in the RJTF. The following points were clarified.

(1) Addition of a short strut was effective for intensive combustion.

(2) There were three modes of engine operation with normal fuel injection.

(a) With a low level of fuel flow rate, weak combustion mainly occurred in the divergent part of the combustor with very small production of thrust.

(b) With a high level of fuel flow rate within the start condition, intensive combustion occurred in the combustor with high combustion efficiency.

(c) When the normally injected fuel flow rate was excessive, the engine was in the unstart condition. The drag was greater than that in the condition with air flow only.

(3) The flame was held in the low-velocity region around the step in the intensive-combustion mode, especially near the cowl. Then, the flame could be held without the plasma ignitors.

(4) Tangential injection with the fuel flow rates employed here was not suitable for the present engine configuration or for the present engine operating conditions.

(5) In the inlet, gradual transition from the start to the unstart condition was not observed. Unstart

seemed to begin with growth of the low-velocity region around the cowl. Re-start from the unstart condition was observed when the fuel flow rate was reduced.

Acknowledgments

The authors thank the members of the scramjet research group of NAL for cooperation in testing, data processing, and discussion. The present study was conducted as a part of the program of NAL-Mitsubishi Heavy Industries LTD. cooperative research.

References

1) Yatsuyanagi, N., Chinzei, N., and Miki, Y. ; Initial Tests of a Sub-Scale Scramjet Engine, *Proceedings of the 12th International Symposium on Air Breathing Engines* (Melbourne, Australia) AIAA, Washing-ton, DC, USA (1995) pp. 1330-1337.

2) Masuya, G., and Chinzei, N. ; Scramjet Engine Tests at Mach 4 and 6, The International Union of Theoretical and Applied Mechanics Symposium on Combustion in Supersonic Flows 7, Poitiers, France (1995／Oct.).

3) Hiraiwa, T., Mitani, T., Izumikawa, M., and Ono, F. ; Calibration Studies of Nozzle Flow in Ramjet Engine Test Facility, The 12th International Symposium on Space Technology and Science, Paper 96-d-14, Gifu, Japan (1996／May).

4) Masuya, G., Kudo, K., Murakami, A., Komuro, T., Tani, K., Kanda, T., Wakamatsu, Y., Chinzei, N., Sayama, M., Ohwaki, K., and Kimura, I. ; Some Governing Parameters of Plasma Torch／Flame-holder in a Scramjet Combustor, *Journal of Propulsion and Power*, Vol.9, No.2 (1993) pp.176-181.

5) Hiraiwa, T., Sato, S., Tomioka, S., Kanda, T., Shimura, T., and Mitani, T. ; Testing of a Scramjet Engine Model in Mach 6 Vitiated Air Flow, AIAA Paper 97-0292 (1997／Jan.).

6) Carslaw, H. S., and Jaeger, J. C. ; Conduction of Heat in Solids (1959) pp.112-113, 2nd ed., Oxford University Press, Oxford, England, UK.

7) Kanda, T., Tani, K., Komuro, T., Murakami, A., Kudo, K., and Chinzei, N. ; Impulse Function and Drag in Scramjet Inlet Models, *Journal of Pro-pulsion and Power*, Vol.12, No.6 (1996) pp.1181-1183.

8) White, F. M. ; Viscous Fluid Flow (1974) pp.632-640, McGraw-Hill, New York, USA.

9) Lamb, J. P. and Oberkampf, W. L. ; Review and Development of Base Pressure and Base Heating Correlations in Supersonic Flow, *Journal of Spacecraft and Rockets*, Vol.32, No.1 (1995) pp.8-23.

10) Karashima, K., and Hasegawa, K., "An Approximate Approach to Base Flow Behind Two-Dimensional Rearward-Facing Steps Placed in a Uniform Supersonic Stream, Institute of Space and Aeronautical Science Report No.501, Tokyo, Japan (1973／Nov.).

11) Waltrup, P. J., Billig, F. S., and Stockbridge, R. D. ; Engine Sizing and Integration Requirements for Hypersonic Airbreathing Missile Applications, AGARD CP-307 (1982).

12) Tani, K., Kanda, T., Kudo, K., Murakami, A., Komuro, T., and Itoh, K. ; Aerodynamic Performance of Scramjet Inlet Models with a Single Strut, AIAA Paper 93-0741 (1993／Jan.).

13) Diskin, G. S., and Northam, G. B. ; Effect of Scale on Supersonic Combustor Performance, AIAA Paper 87-2164 (1987／Jun.-Jul.).

14) Wagner, T. C., O'Brien, W. F., Northam, G. B., and Eggers, J. M. ; Design and Evaluation of a New Injector Configuration for Supersonic Combustion, *Proceedings of the Eighth International Symposium on Air Breathing Engines*, AIAA, Cincinnati, OH, USA (1987) pp. 390-397.

15) Huber, P. W., Schexnayder, Jr., C. J., and McClinton, C. R. ; Criteria for Self-Ignition of Supersonic Hydrogen-Air Mixtures, NASA TP-1457 (1979).

16) Billig, F. S., Orth, R. C., and Lasky, M. ; A Unified Analysis of Gaseous Jet Penetration, AIAA *Journal*, Vol.9, No.6 (1971) pp. 1048-1057.

17) Billig, F. S. ; Shock-Wave Shapes around Spherical- and Cylindrical-Nosed Bodies, *Journal of Spacecraft and Rockets*, Vol.4, No.6 (1967) pp. 822-823.

18) Tani, K., Kanda, and T., Tokunaga, T. ; Starting Characteristics of Scramjet Inlets, *Proceedings of the 11th International Symposium on Air Breathing Engines*, AIAA, Tokyo, Japan (1993) pp. 1071-1080.

19) Komuro, T., Kudo, K., Masuya, G., Chinzei, N., Murakami, A., and Tani, K. ; Experimant on a Rectangular Cross Section Scramjet Combustor, NAL TR-1068 (1990／Jun.) (in Japanese).

20) Chinzei, N., Komuro, T., Kudou, K., Murakami, A., Tani, K., Masuya, G., and Wakamatsu, Y. ; Effects of Injector Geometry on Scramjet Combustor Perfor-

mance, *Journal of Propulsion and Power*, Vol.9, No.1 (1993) pp.146-152.

21) Murakami, A., Komuro, T., and Kudo, K. ; Experiment on a Rectangular Cross Section Scramjet Combustor (II)- Effects of Fuel Injector Geometry-, NAL TR- 1220 (1993／Dec.) (in Japanese).

22) Waltrup, P. J., and Billig, F. S. ; Prediction of Precombustion Shock Wall Pressure Distributions in Scramjet Engines, *Journal of Spacecraft and Rockets*, Vol.10, No.9 (1973) pp.620-622.

23) Sunami, T., Sakuranaka, N., Tani, K., Hiraiwa, T., and Shimura, T. ; Mach 4 Tests of a Scramjet Engine - Effect of Isolator, to be presented at the 13*th International Symposium on Air Breathing Engines*, AIAA, Chattanooga, TN, USA (1997／Sep.).

24) Sato, S., Izumikawa, M., Tomioka, S., and Mitani, T. ; Scramjet Engine Test at the Mach 6 Flight Condition, to be presented at the 33rd AIAA／ASME／SAE／ASEE Joint Propulsion Conference, AIAA, Seattle, WA, USA (1997／Jul.).